

Specific Heat Capacity Determination by DSC

April 19, 10:00am - 11:00am EDT

Specific heat capacity (c_p) is an important, temperature-dependent material property and is often specified in material data sheets. It is a key property for improving technical processes such as injection molding, spray drying, or crystallization, as well as for the safety analysis of chemical processes and the design of chemical reactors.

Watch this session during the WAS Virtual Conference:



Dr. Jürgen Schawe

[Register Now](#)

Piezoelectric Strain Control of Terahertz Spin Current

Avinash Chaurasiya, Ziqi Li, Rohit Medwal,* Surbhi Gupta, John Rex Mohan, Yasuhiro Fukuma, Hironori Asada, Elbert E. M. Chia,* and Rajdeep Singh Rawat*

Electrical control of photogenerated terahertz (THz) spin current pulses from a spintronic emitter has been at the forefront for the development of scalable, cost-efficient, wideband optospintronic devices. Artificially combined ferroelectric and ferromagnet heterostructure provides the potential avenue to deterministically control the phase of THz spin current pulse through piezoelectric strain. Here, the electric field-mediated piezoelectric strain control of photogenerated THz spin current pulse from a multiferroic spintronic emitter is demonstrated. The phase reversal of the THz spin current pulse is obtained from the combined effect of piezoelectric strain and a small magnetic field applied opposite to the initial magnetization of the ferromagnet. The piezoelectric strain-controlled phase switching of THz spin current thus opens a door to develop efficient strain engineered scalable on-chip THz spintronics devices.

1. Introduction

Artificial multiferroic systems, consisting of ferroelectric (FE) and ferromagnetic (FM) orders,^[1–6] provide a unique approach to control the ferromagnetic order by electric field or the ferroelectric order using magnetic field^[7,8] due to their magnetolectric coupling.^[8,9] Utilizing magnetolectric coupling in multiferroic FE/FM heterostructures, the active manipulation of various processes has been demonstrated^[8,10–15] but the active manipulation of ultrafast terahertz (THz) spin dynamics and associative superdiffusive processes remain unexplored. The recent progress in THz spintronics suggests a typical ferromagnet (FM)/heavy

metal (HM) heterostructure upon illumination by a femtosecond (fs) laser pulse drives the spins out of equilibrium^[16] in the FM layer causing the ultrafast demagnetization^[17–19] and ballistic superdiffusion of spins^[20] into the adjacent HM layer,^[20,21] generating a transient charge current through the spin to charge conversion process of inverse spin Hall effect (ISHE).^[22–24] This transient charged current, which exists in the sub-picosecond (ps) timescale, emits THz electromagnetic radiation according to Maxwell's equation.^[17,25,26] Achieving the active control of such sub-picosecond THz spin current pulses and the resulting THz radiation pulse emitted from the fs photoexcitation of THz spintronic emitter is highly desirable to fabricate the on-chip optospintronic devices for potential applications in high-speed computing^[27] and memory devices with different functionalities.^[28] Several other systems have also been opted to design terahertz emitters such as shift current-based system,^[29] Rashba-type interfaces,^[30] ferromagnetic/antiferromagnetic interface-based system,^[31] cross-bar design consisting of ferromagnet with positive and negative spin Hall materials for coding and programmable devices.^[32] The control of the THz spin current through electrical current,^[33] magnetic field,^[34,35] photothermal effect,^[36] anisotropy modulation,^[37] and helicity of light^[34] have been demonstrated. However, the deterministic control of phase of THz spin current pulse through piezoelectric strain, using electric field, has not been explored to date.

In this article, we design an artificial multiferroic spintronic emitter (Cu/Pb(Mg_{1/3}Nb_{2/3})O₃-0.31PbTiO₃(PMN-PT)/NiFe/Pt) to demonstrate the piezoelectric strain control of the THz spin current pulse amplitude as well as the phase switching. The sequential cyclic sweep of applied electric field (*E*) and corresponding measurements of strain, remanent magnetization

A. Chaurasiya, R. Medwal, S. Gupta, R. S. Rawat
 Natural Sciences and Science Education
 National Institute of Education
 Nanyang Technological University
 Singapore 637616, Singapore
 E-mail: rohit.medwal@nie.edu.sg; rajdeep.rawat@nie.edu.sg

Z. Li, E. E. M. Chia
 Division of Physics and Applied Physics
 School of Physical and Mathematical Sciences
 Nanyang Technological University
 21 Nanyang Link, Singapore 637371, Singapore
 E-mail: elbertchia@ntu.edu.sg

R. Medwal
 Department of Physics
 Indian Institute of Technology Kanpur
 Kanpur, Uttar Pradesh 208016, India

J. R. Mohan, Y. Fukuma
 Department of Physics and Information Technology
 Kyushu Institute of Technology
 Iizuka 820-8502, Japan

Y. Fukuma
 Research Center for Neuromorphic AI Hardware
 Kyushu Institute of Technology
 Kitakyushu 808-0196, Japan

H. Asada
 Graduate School of Sciences and Technology for Innovation
 Yamaguchi University
 Ube 755-8611, Japan

 The ORCID identification number(s) for the author(s) of this article can be found under <https://doi.org/10.1002/adom.202201929>.

© 2022 The Authors. Advanced Optical Materials published by Wiley-VCH GmbH. This is an open access article under the terms of the Creative Commons Attribution License, which permits use, distribution and reproduction in any medium, provided the original work is properly cited.

DOI: 10.1002/adom.202201929

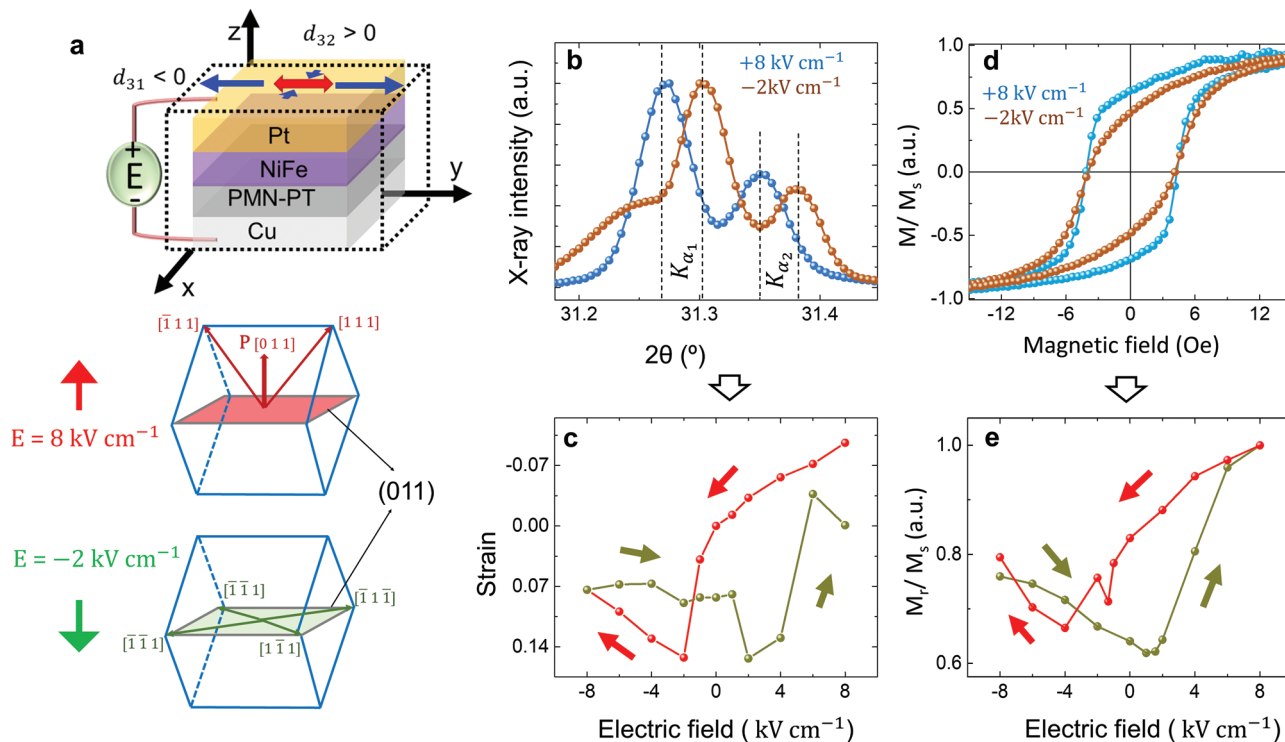


Figure 1. Electric field control of strain and effective magnetization. a) Schematic of the artificial multiferroic heterostructured spintronic device stack with the applied electric field. The middle and bottom schematics show the rhombohedral unit cells of the PMN-PT at maximum (+8 kV cm⁻¹) and minimum strained (-2 kV cm⁻¹) states. b) X-ray diffraction patterns about (011) diffraction peak at maximum and minimum strained states in the PMN-PT (011) single crystal. c) *Strain-E* butterfly hysteresis for a PMN-PT (011) substrate. d) *M-H* hysteresis recorded at maximum and minimum strained states. e) Variation of the remanent magnetization, M_r/M_s , with the applied electric field (*M-E* butterfly hysteresis).

(M_r/M_s), and emitted THz radiation pulse amplitude exhibit the remarkable correlated nonlinear butterfly hysteresis in *Strain-E*, *M-E*, and *THz-E* curves indicating simultaneous control and probing of strain dynamics, remanent magnetization, and THz spin dynamics. The observed inversion of both the “*THz-E* butterfly hysteresis” and the magnetization versus magnetic field (*M-H*) hysteresis curves upon changing the measurements configuration from easy-axis to the hard-axis of magnetization (with in-plane rotation of the sample), clearly demonstrates that the manipulation of the emitted THz radiation pulse is due to the piezoelectric strain control of magnetic anisotropy of NiFe layer. The phase switching of the emitted THz radiation pulse is demonstrated using the combined effect of electric field-induced strain and a small magnetic field applied opposite to the initial magnetization direction of the NiFe layer. This phase switching of THz spin current using piezoelectric strain in artificial multiferroic heterostructures is a milestone step forward for strain engineered on-chip THz spintronics devices.

2. Results and Discussion

To demonstrate the electric field control of THz spin current in an artificial multiferroic spintronic emitter via strain-mediated manipulation of the effective magnetization, a heterostructured stack of electrode/FE/FM/HM (Cu/PMN-PT/NiFe/Pt)

has been designed (refer the Experimental section for fabrication details), as shown in **Figure 1a**. The externally applied electric field across the device stack induces strain that causes respective compression and elongation along *x*- and *y*-directions ascribed to negative ($d_{31} < 0$) and positive ($d_{32} > 0$) piezoelectric charge coefficients along these directions. **Figure 1a** also shows the schematics of the unit cells of rhombohedral (0 1 1) PMN-PT, poled perpendicular to (0 1 1) plane, and their corresponding maximum strained state at +8 kV cm⁻¹ along [0 1 1] with net out-of-plane polarization, solid red arrow, and minimum strained state at coercive electric field, E_c , of -2 kV cm⁻¹ along [0 $\bar{1}$ 1] with zero net polarization. These electric field values, required to attain maximum and minimum strained states, are estimated from in-situ X-ray diffraction (XRD) measurements of the PMN-PT. The XRD spectra at +8 kV cm⁻¹ and coercive electric field of -2 kV cm⁻¹ in **Figure 1b**, with maximum shift in the (0 1 1) diffraction peak, correspond to the maximum and minimum strained states of the device, respectively. Furthermore, to obtain the variation of the strain, calculated from the shift in (0 1 1) $K_{\alpha 1}$ diffraction peak, the XRD measurements were performed with the cyclic sweep of electric field as shown in **Figure 1c**. The XRD patterns obtained at various electric field applied in cyclic order, from +8 kV cm⁻¹ → -8 kV cm⁻¹ → +8 kV cm⁻¹, are shown in the Supporting Information section S1. **Figure 1c** shows a butterfly loop-like behavior (*Strain-E* hysteresis), wherein maximum-strained (at +8 kV cm⁻¹) and minimum-strained (at coercive

field of -2 kV cm^{-1} states can be identified for electric field sweep from $+8$ to -8 kV cm^{-1} .

The induced strain is utilized to control the remanent magnetization of NiFe layer through magnetoelectric coupling between PMN-PT and NiFe. The change in M_r/M_s of NiFe layer is investigated using vibrating sample magnetometer (VSM). Figure 1d shows the change in remanent magnetization observed from M-H hysteresis for maximum and minimum strained states, confirming the modulation of effective magnetization of NiFe layer by an applied electric field-induced strain. The M-H hysteresis for various strained states, for the cyclic variation of applied electric field from $-8 \text{ kV cm}^{-1} \rightarrow +8 \text{ kV cm}^{-1} \rightarrow -8 \text{ kV cm}^{-1}$, are given in the Supporting Information section S2a. It is observed that the cyclic variation of the M_r/M_s obtained from analyzing M-H hysteresis with the applied electric field also follows a

butterfly behavior (M - E hysteresis), see Figure 1e, similar to the $Strain$ - E hysteresis. The maximum and minimum values of the M_r/M_s are observed at ± 8 and $\pm 2 \text{ kV cm}^{-1}$, respectively, which is in direct correlation with the strain in the device. The electric field control of effective magnetization is also confirmed using ferromagnetic resonance spectroscopy measurements, are given in the Supporting Information section S2b. Therefore, the applied electric field can simultaneously control the strain and effective magnetization in the device.

After the confirmation of the electric field-induced strain control of remanent magnetization, the piezoelectric strain manipulation of the magnitude and phase of the emitted THz pulses is probed using THz time domain spectroscopy setup shown in Figure 2a (refer the Experimental section for setup). Figure 2b shows the schematic of the device with mechanism

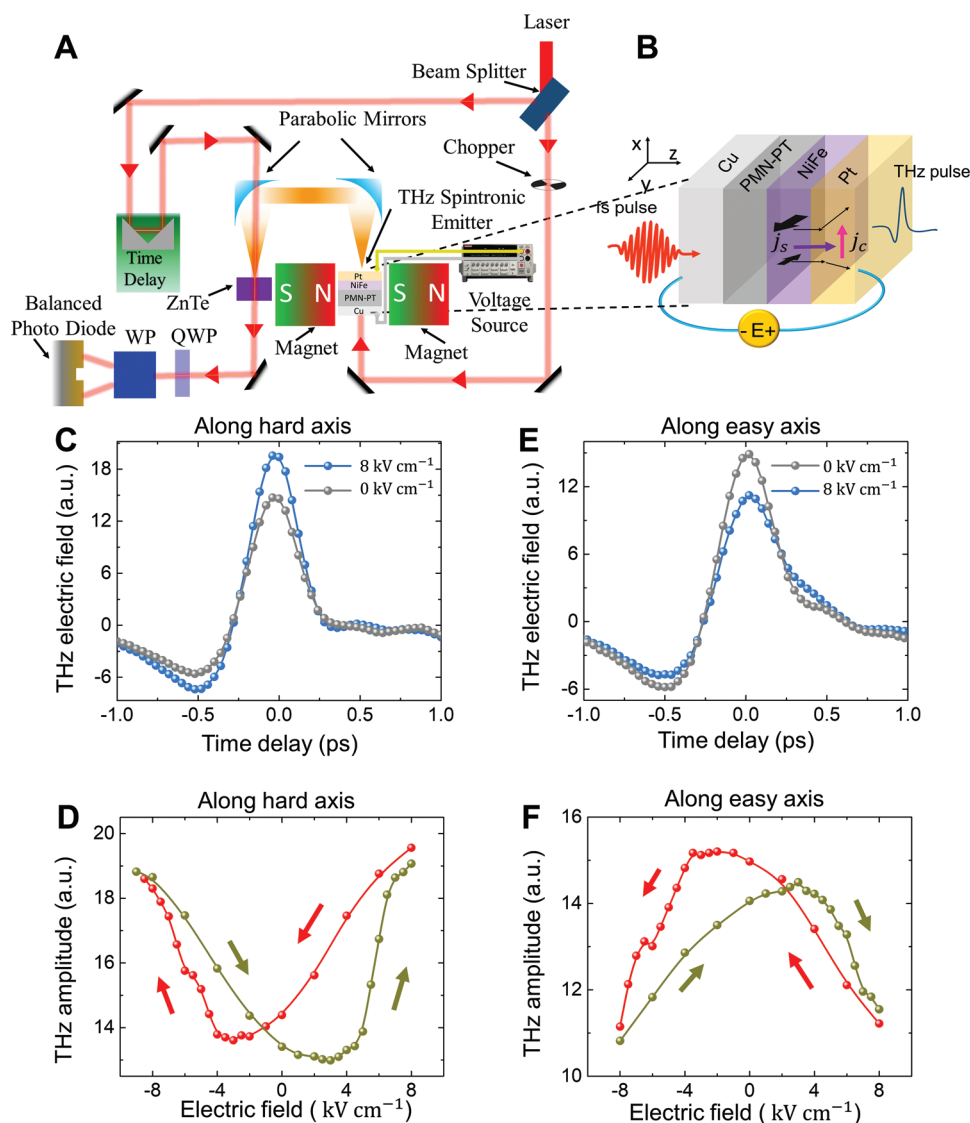


Figure 2. Electric field control of THz spin current at remanent magnetization. a) Schematic of the setup for measurement and generation of THz radiation, at 1.2 mJ cm^{-2} pump fluence. b) Schematic of the artificial multiferroic spintronic emitter with the mechanism for emission of THz spin current. c) Emitted THz spin current at applied electric field of 0 and $+8 \text{ kV cm}^{-1}$, for measurements set along hard axis of magnetization of NiFe. d) THz - E butterfly hysteresis along the hard axis of magnetization of NiFe. e) Emitted THz spin current at applied electric field of 0 and $+8 \text{ kV cm}^{-1}$, for measurements set along easy axis of NiFe. f) THz - E butterfly hysteresis along the easy axis of magnetization of NiFe.

of THz radiation emission. Here, the photoexcitation leads to ultrafast demagnetization and ballistic superdiffusion of spins in NiFe/Pt system at sub-ps time scale, which results in the injection of THz spin current (j_s) pulse from the NiFe to the Pt layer, where the j_s is converted into a charge current (j_c) pulse through the ISHE, according to $j_c = \gamma j_s \times M/|M|^{28}$ with γ as spin Hall angle and M being the magnetization of the ferromagnet. The transient THz charge current in the Pt layer results in the emission of THz radiation, which is recorded to probe the characteristics of photogenerated THz spin currents at different applied electric field. Figure 2c shows the emitted THz radiation pulses at the maximum strained (+8 kV cm⁻¹) and unstrained (0 kV cm⁻¹) states, at remanent magnetization, for measurements along the magnetization hard-axis (H.A.) of NiFe. The identification of hard/easy axis of magnetization of NiFe layer is done by carefully analyzing the emitted THz pulse amplitudes for maximum strained and unstrained states at different orientations of the sample. The significant enhancement in the amplitude of the emitted THz pulse at maximum strained state (+8 kV cm⁻¹) in comparison with the zero electric field state, in Figure 2c, is due to the enhancement in the remanent magnetization of the NiFe layer, which leads to the manipulation of the spin current j_s , ballistically diffusing in the Pt layer, generating a charged current j_c and hence changing the amplitude of the emitted THz radiation. Furthermore, to verify the piezoelectric strain control of THz amplitude the emitted THz radiation pulses were recorded by sweeping the electric field in cyclic order from +8 kV cm⁻¹ → -8 kV cm⁻¹ → +8 kV cm⁻¹. The emitted THz radiation pulse signal recorded at different applied electric fields are presented in the Supporting Information section S3. The plot of THz radiation pulse amplitude as a function of applied electric field, in Figure 2d, exhibits a nonlinear butterfly loop-like curve, which we have termed as “THz-E butterfly hysteresis.” The obtained “THz-E butterfly hysteresis,” in Figure 2d, is in direct correlation with the *Strain-E* and *M-E* butterfly hysteresis shown in Figure 1c,e, respectively. This demonstrates the simultaneous electric field control of the strain, the M_r/M_s and the THz pulse amplitude in multiferroic optospintronic emitter.

Thereafter, the device is rotated in the plane toward the easy-axis of magnetization of NiFe layer to investigate the THz radiation emission for different electric field at remanent magnetization. Figure 2e shows the THz pulse signals at maximum strained and unstrained states of the device for this orientation. The THz pulse signals recorded for various other strained states are shown in the Supporting Information section S4. The significant decrease in the THz pulse amplitude at maximum strained state in comparison with unstrained state is due to the decrease in the remanent magnetization, which leads to injection of lower spin current j_s from NiFe to Pt layer thus smaller j_c . The variation in THz pulse amplitude with the electric field swept in cyclic order from +8 kV cm⁻¹ → -8 kV cm⁻¹ → +8 kV cm⁻¹ is plotted in Figure 2f, which also exhibits butterfly loop-like hysteresis. It is observed that the “THz-E butterfly hysteresis loop” in Figure 2f is inverted in comparison with the one shown in Figure 2d.

To understand the origin of the inversion of “THz-E butterfly hysteresis” (Figure 2d,f), *M-H* measurements were performed using VSM (vibration sample magnetometry). First, the easy

and the hard axes of magnetization of NiFe layer were identified using VSM measurement by in-plane rotation of the sample in step size of 10°. Figure 3a shows the variation of the normalized remanent magnetization with the complete in-plane rotation of the sample from 0° to 360° in the absence of electric field. Here, it is evident that the sample has the easy axis along 90° and 270° and the hard axis along 0° and 180°, as shown in Figure 3b. After finding the easy and hard axes of magnetization of NiFe layer, the *M-H* hysteresis measurement was performed at different applied electric fields. Initially, we set the sample position along the hard axis of magnetization and performed the *M-H* hysteresis measurements at 0 and +8 kV cm⁻¹, shown in Figure 3c. The schematic showing the meaning of measurement along the easy axis and measurement along the hard axis is shown in the Supporting Information section S5. It is observed that at +8 kV cm⁻¹, the M_r/M_s (normalized remanent magnetization, marked by dotted line in Figure 3c) of the *M-H* hysteresis loop increases in comparison with the hysteresis loop at 0 kV cm⁻¹, which is in direct correlation with the observed increase in the emitted THz radiation pulse amplitude observed in Figure 2c. The increase in the squareness, M_r/M_s ratio, of *M-H* hysteresis loop from unstrained to maximum strained state also indicates the control of effective magnetization of NiFe. The sample is then rotated by 90° to align it along the easy axis of magnetization and corresponding *M-H* hysteresis measurements at the electric fields of 0 and +8 kV cm⁻¹ are shown in Figure 3d. A reverse trend, with a decrease in M_r/M_s value at +8 kV cm⁻¹ in comparison with the 0 kV cm⁻¹, is observed, which is consistent with the smaller THz amplitude observed in Figure 2e for this orientation, leading to the inversion of “THz-E butterfly hysteresis.” The decrease in the squareness of *M-H* hysteresis loop from unstrained to maximum strained state indicates the control of easy axis of magnetization of NiFe. This confirms that the THz spin current pulse amplitude is manipulated by the control of easy axis of magnetization of NiFe layer under piezoelectric strain-modulated magnetic anisotropy in multiferroic THz spintronic emitter.

As we know the magnetization in most of the magnetostrictive materials is difficult to be switched by piezoelectric strain alone, for phase reversal of THz spin current pulse and hence a suitable combination of electric and magnetic field needs to be used. To deduce the suitable combination of electric and magnetic field values for THz pulse-phase reversal, the *THz-H* hysteresis were plotted by recording the peak amplitude of the THz radiation pulse at different applied magnetic field values for zero and 10 kV cm⁻¹ electric fields, as shown in Figure 4a. The whole set of *THz-H* hysteresis measurements for different applied electric field values is given in the Supporting Information section S6. The measured *THz-H* hysteresis at different applied electric field values further confirms the control of THz amplitude at remanent magnetic field. In addition to the control over the THz pulse amplitude, the piezoelectric strain combined with the laser-heating effect gives the control of the magnetic coercivity and remanent terahertz amplitude as seen in Figure 4a and in the Supporting Information section S6.

THz-H hysteresis loops at +0 and 10 kV cm⁻¹ in Figure 4a suggest that the phase of the THz spin current pulse can be switched at a selective small applied magnetic field opposite to the initial magnetization of NiFe. It is found that at magnetic

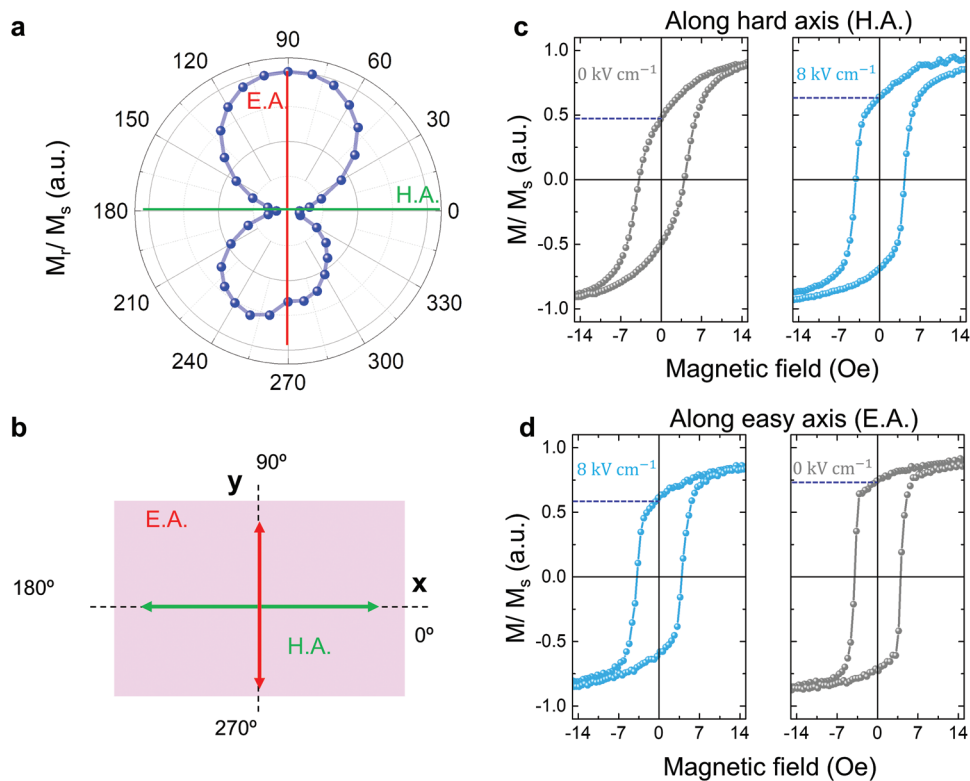


Figure 3. Piezoelectric strain control of remanent magnetization. a) Variation of normalized remanent magnetization as a function of in-plane rotation of sample. b) Schematic of the easy and hard axes of magnetization in a sample plane. c) $M-H$ hysteresis along hard axis of the magnetization at 0 and +8 kV cm^{-1} . d) $M-H$ hysteresis along easy axis of the magnetization at 0 and +8 kV cm^{-1} . The dotted horizontal line in: c,d) indicates the normalized remanent magnetization, M_r/M_s , which changes with the change in applied electric field.

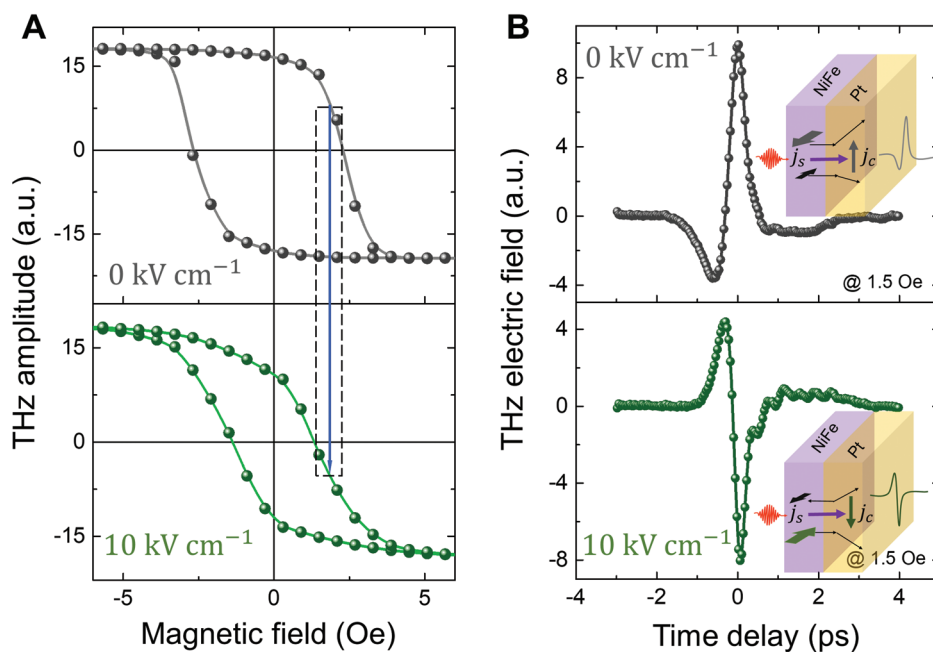


Figure 4. Electric field-controlled phase switching of THz spin current pulse. a) THz- H hysteresis loop at 0 and 10 kV cm^{-1} . The blue arrow marks the applied magnetic field value of +1.5 Oe, in the direction opposite to initial magnetization direction of FM layer where the THz pulse phase reversal should be observed, as shown in (b). The dotted box marks the region between the coercive field points depicting the magnetic field range, opposite to initial magnetization direction, with in which the phase reversal can be achieved. b) Phase switching of the THz pulse with the change in electric field from 0 to 10 kV cm^{-1} at small applied magnetic field of +1.5 Oe.

field of 1.5 Oe, marked by blue arrow in Figure 4a, the phase of the THz pulse can be reversed just by switching the electric field from 0 to 10 kV cm⁻¹, as shown in Figure 4b. The applied magnetic field of 1.5 Oe is not unique, rather it exists in a range from 1.3 to 2.3 Oe between the coercive magnetic field values of THz-*H* hysteresis for 0 and 10 kV cm⁻¹. It may be noted; however, that the switching of the electric field from 10 to 0 kV cm⁻¹ does not reverse the phase back to the initial state. This is because the direction and magnitude of the magnetic field remains the same, 1.5 Oe, and the piezoelectric strain manipulates the effective magnetization in the direction same as that of 1.5 Oe. The phase reversal of the emitted THz spin current can, however, be realized again if the direction of the applied magnetic field is reversed.

In summary, we demonstrate piezoelectric strain control of THz spin current pulse in a multiferroic spintronic emitter where the strain manipulates the injected spin current from FM to HM layer by controlling the effective magnetization due to the change in magnetic anisotropy of the FM layer. Moreover, the combined effect of strain and magnetic field switches the phase of the emitted THz pulse by reversal of the effective magnetization of the FM. Our results of strain-engineered emitted THz radiation have far-reaching implications for research on multiferroics, ultrafast magnetism, and THz science. The experiments demonstrate a novel methodology to probe and control the spin and strain dynamics by correlating them with emitted THz radiation from the multiferroic spintronic emitter in ultrafast timescales. Piezoelectric strain-controlled photogenerated THz spin current thus opens a door to develop futuristic high-speed optospintronic devices for computing and communication technologies.

3. Experimental Section

Device Fabrication: A ferroelectric (011) PMN-PT substrate, with both side-polished surfaces was used to fabricate the THz spintronic device. The NiFe (5 nm) and Pt (5 nm) thin films were deposited on PMN-PT, in that order, by electron beam at the base pressure of 10⁻⁶ Pa. The deposition rate of the NiFe was kept 0.025 Å s⁻¹ while for Pt, the deposition rate was kept at 0.03 Å s⁻¹. The chamber pressure during the deposition was 1.68–1.84 × 10⁻⁵ Pa. For the capacitive configuration device fabrication, the Cu electrode was deposited on the bottom surface of the PMN-PT using 50 W DC magnetron sputtering at an argon pressure of 3 mTorr. The quality of the NiFe/Pt bilayer and NiFe thin film was characterized using the ferromagnetic resonance (see Section S10 in Supporting Information). The value of effective magnetization and damping coefficient extracted from the measurement were found to be 820 mT and 0.022 demonstrating the good quality of the NiFe/Pt bilayer and NiFe thin film.

Vibrating Sample Magnetometer (VSM) Measurements: The *M-H* hysteresis measurements were performed using Lakeshore VSM. The electrical connections to the top (Pt) and bottom (Cu) electrodes were made using the Cu wire and the electric field was applied across the thickness of the device using Keithley 2410 source meter during VSM measurements.

***I-V* Measurements:** The *I-V* characteristic of the device was performed using the Keithley 2410 source meter at room temperature as well as at different laser pump fluence. The laser-heating effect on the coercive electric field was observed and given in the Supporting Information section S7.

X-Ray Diffraction: High resolution out of plane X-ray diffraction measurement were performed on (011) PMN-PT substrate at different

applied electric field using the Keithley 2410 source meter by a Bruker D8 Discover diffractometer (Cu K_α X-ray source) setup.

THz Generation and Measurement Setup: A Ti:sapphire ultrafast amplifier (Legend Coherent, 800 nm, ≈50 fs, 1 kHz) was employed in this setup. The generated laser pulses were split into two optical paths by a pellicle beam splitter: One was used to pump at normal incidence and generate spin-polarized carriers and the other portion of the laser beam was used for THz detection. The THz pulses generated were projected onto the x-axis (vertical) by using a wire-grid THz polarizer, and then collected and focused by two parabolic mirrors onto a 1 mm thick <110> ZnTe crystal for free-space electro-optic sampling. The magnetic field direction was controlled by a motorized rotational stage (Thorlabs PRM1/MZ8). All measurements were performed at room temperature in dry air with a humidity less than 2%.

THz-E Hysteresis Measurement: To observe the THz-*E* hysteresis curves, the emitted THz pulses were recorded at different applied electric field. The electric field was applied using the Keithley 2410 source meter. Variation of the THz pulse amplitude with the applied electric field gave the THz-*E* butterfly-like hysteresis curve.

Supporting Information

Supporting Information is available from the Wiley Online Library or from the author.

Acknowledgements

A.C. acknowledges the NTU-Research Scholarship (NTU-RSS). R.M., S.G., and R.S.R. acknowledge the support from the Ministry of Education, Singapore (grant No. MOE2019-T2-1-058) (ARC 1/19 RSR) and National Research Foundation (grant No. NRF-CRP21-2018-0003). Z.L. and E.E.M.C. acknowledge the support from the Singapore Ministry of Education AcRF Tier 3 Programme “Geometrical Quantum Materials” (grant No. MOE2018-T3-1-002) and Singapore National Research Foundation Competitive Research Programme “The Next Generation of Spintronics with 2D Heterostructures” (grant No. NRF-CRP22-2019-0004). Y.F. also acknowledges the JSPS Grant-in-Aid (KAKENHI Nos. 18H01862a and 19K21112).

Conflict of Interest

The authors declare no conflict of interest.

Author Contribution

A.C. and Z.L. contributed equally to this work. R.M., A.C., and R.S.R. conceived the idea. A.C., R.M., Z.L., E.E.M.C., and R.S.R. designed the experiments. Z.L. and A.C. performed the terahertz measurements under the supervision of E.E.M.C. A.C. and Z.L. analyzed the THz data. R.M., S.G., J.R.M., H.A., and Y.F. fabricated the spintronic emitter. A.C. performed the electric field modulated XRD, FMR, and VSM measurements under the supervision of R.M. and R.S.R. E.E.M.C. and R.S.R. colead the overall project. All the authors analyzed and discussed the results. A.C., R.M., and R.S.R. wrote the manuscript with inputs from all the authors.

Data Availability Statement

The data that support the findings of this study are available from the corresponding author upon reasonable request.

Keywords

ferroelectric/ferromagnet/heavy metal heterostructure, multiferroic spintronic emitter, phase reversal, piezoelectric strain, THz spin current

Received: August 18, 2022

Revised: September 27, 2022

Published online: October 26, 2022

- [1] M. Ghidini, R. Mansell, F. Maccherozzi, X. Moya, L. C. Phillips, W. Yan, D. Pesquera, C. H. W. Barnes, R. P. Cowburn, J.-M. Hu, S. S. Dhesi, N. D. Mathur, *Nat. Mater.* **2019**, *18*, 840.
- [2] Na Lei, T. Devolder, G. Agnus, P. Aubert, L. Daniel, J.-V. Kim, W. Zhao, T. Trypiniotis, R. P. Cowburn, C. Chappert, P. Lecoeur, *Nat. Commun.* **2013**, *4*, 1378.
- [3] D. Pesquera, E. Khestanova, M. Ghidini, S. Zhang, A. P. Rooney, F. Maccherozzi, P. Riego, S. Farokhipoor, J. Kim, X. Moya, M. E. Vickers, N. A. Stelmashenko, S. J. Haigh, S. S. Dhesi, N. D. Mathur, *Nat. Commun.* **2020**, *11*, 3190.
- [4] S. Zhang, Y. G. Zhao, P. S. Li, J. J. Yang, S. Rizwan, J. X. Zhang, J. Seidel, T. L. Qu, Y. J. Yang, Z. L. Luo, Q. He, T. Zou, Q. P. Chen, J. W. Wang, L. F. Yang, Y. Sun, Y. Z. Wu, X. Xiao, X. F. Jin, J. Huang, C. Gao, X. F. Han, R. Ramesh, *Phys. Rev. Lett.* **2012**, *108*, 137203.
- [5] A. Chaurasiya, P. Pal, J. V. Vas, D. Kumar, S. N. Piramanayagam, A. K. Singh, R. Medwal, R. S. Rawat, *Ceram. Int.* **2020**, *46*, 25873.
- [6] R. K. Zheng, C. Chao, H. L. W. Chan, C. L. Choy, H. S. Luo, *Phys. Rev. B* **2007**, *75*, 024110.
- [7] M. Fiebig, T. Lottermoser, D. Meier, M. Trassin, *Nat. Rev. Mater.* **2016**, *1*, 16046.
- [8] T. Zhao, A. Scholl, F. Zavaliche, K. Lee, M. Barry, A. Doran, M. P. Cruz, Y. H. Chu, C. Ederer, N. A. Spaldin, R. R. Das, D. M. Kim, S. H. Baek, C. B. Eom, R. Ramesh, *Nat. Mater.* **2006**, *5*, 823.
- [9] Y.-H. Chu, L. W. Martin, M. B. Holcomb, M. Gajek, S.-J. Han, Q. He, N. Balke, C.-H. Yang, D. Lee, W. Hu, Q. Zhan, P.-L. Yang, A. Fraile-Rodríguez, A. Scholl, S. X. Wang, R. Ramesh, *Nat. Mater.* **2008**, *7*, 478.
- [10] K. Cai, M. Yang, H. Ju, S. Wang, Y. Ji, B. Li, K. W. Edmonds, Yu Sheng, B. Zhang, N. Zhang, S. Liu, H. Zheng, K. Wang, *Nat. Mater.* **2017**, *16*, 712.
- [11] R. O. Cherifi, V. Ivanovskaya, L. C. Phillips, A. Zbelli, I. C. Infante, E. Jacquet, V. Garcia, S. Fusil, P. R. Briddon, N. Guiblin, A. Mougín, F. Kronast, S. Valencia, B. Dkhil, M. Bibes, *Nat. Mater.* **2014**, *13*, 345.
- [12] D. Chiba, M. Sawicki, Y. Nishitani, Y. Nakatani, F. Matsukura, H. Ohno, *Nature* **2008**, *455*, 515.
- [13] X. Chen, X. Zhou, R. Cheng, C. Song, J. Zhang, Y. Wu, Y. Ba, H. Li, Y. Sun, Y. You, Y. Zhao, F. Pan, *Nat. Mater.* **2019**, *18*, 931.
- [14] H. Yan, Z. Feng, S. Shang, X. Wang, Z. Hu, J. Wang, Z. Zhu, H. Wang, Z. Chen, H. Hua, W. Lu, J. Wang, P. Qin, H. Guo, X. Zhou, Z. Leng, Z. Liu, C. Jiang, M. Coey, Z. Liu, *Nat. Nanotechnol.* **2019**, *14*, 131.
- [15] Z. Q. Liu, H. Chen, J. M. Wang, J. H. Liu, K. Wang, Z. X. Feng, H. Yan, X. R. Wang, C. B. Jiang, J. M. D. Coey, A. H. MacDonald, *Nat. Electron.* **2018**, *1*, 172.
- [16] L. Cheng, X. Wang, W. Yang, J. Chai, M. Yang, M. Chen, Y. Wu, X. Chen, D. Chi, K. E. J. Goh, J.-X. Zhu, H. Sun, S. Wang, J. C. W. Song, M. Battiato, H. Yang, E. E. M. Chia, *Nat. Phys.* **2019**, *15*, 347.
- [17] A. Eschenlohr, M. Battiato, P. Maldonado, N. Pontius, T. Kachel, K. Hollmack, R. Mitzner, P. M. Oppeneer, C. Stamm, *Nat. Mater.* **2013**, *12*, 332.
- [18] J.-Y. Bigot, M. Vomir, L. H. F. Andrade, E. Beaurepaire, *Chem. Phys.* **2005**, *318*, 137.
- [19] J.-Y. Bigot, M. Vomir, E. Beaurepaire, *Nat. Phys.* **2009**, *5*, 515.
- [20] M. Battiato, K. Carva, P. M. Oppeneer, *Phys. Rev. Lett.* **2010**, *105*, 027203.
- [21] N. Berggaard, M. Hehn, S. Mangin, G. Lengaigne, F. Montaigne, B. Koopmans, G. Malinowski, *Phys. Rev. Lett.* **2016**, *117*, 147203.
- [22] S. Gupta, R. Medwal, D. Kodama, K. Kondou, Y. Otani, Y. Fukuma, *Appl. Phys. Lett.* **2017**, *110*, 022404.
- [23] U. Shashank, R. Medwal, T. Shibata, R. Nongjai, J. V. Vas, M. Duchamp, K. Asokan, R. S. Rawat, H. Asada, S. Gupta, Y. Fukuma, *Adv. Quantum Technol.* **2020**, *4*, 2000112.
- [24] Z. Fang, H. Wang, X. Wu, S. Shan, C. Wang, H. Zhao, C. Xia, T. Nie, J. Miao, C. Zhang, W. Zhao, Li Wang, *Appl. Phys. Lett.* **2019**, *115*, 191102.
- [25] T. Kampfrath, M. Battiato, P. Maldonado, G. Eilers, J. V. Zbarsky, F. Freimuth, Y. Mokrousov, M. Wolf, I. Radu, P. M. Oppeneer, *Nat. Nanotechnol.* **2013**, *8*, 256.
- [26] T. Seifert, S. Jaiswal, U. Martens, J. Hannegan, L. Braun, P. Maldonado, F. Freimuth, A. Kronenberg, J. Henrizi, I. Radu, E. Beaurepaire, Y. Mokrousov, P. M. Oppeneer, M. Jourdan, G. Jakob, D. Turchinovich, L. M. Hayden, M. Wolf, T. Kampfrath, *Nat. Photonics* **2016**, *10*, 483.
- [27] A. V. Chumak, V. Á. I. Vasyuchka, A. Á. A. Serga, B. Hillebrands, *Nat. Phys.* **2015**, *11*, 453.
- [28] L. J. Cornelissen, J. Liu, R. A. Duine, J. B. Youssef, B. J. Van Wees, *Nat. Phys.* **2015**, *11*, 1022.
- [29] M. Tong, Y. Hu, W. He, X.-L. Yu, S. Hu, T. Jiang, *ACS Nano* **2021**, *15*, 17565.
- [30] M. Tong, Y. Hu, Z. Wang, T. Zhou, X. Xie, T. Jiang, *Nano Lett.* **2020**, *21*, 60.
- [31] C. Li, B. Fang, L. Zhang, Q. Chen, X. Xie, N. Xu, Z. Zeng, Z. Wang, L. Fang, T. Jiang, *Phys. Rev. Appl.* **2021**, *16*, 024058.
- [32] M. Tong, Y. Hu, W. He, S. Hu, T. Jiang, *ACS Nano* **2022**, *16*, 8294.
- [33] M. Chen, Y. Wu, Y. Liu, K. Lee, X. Qiu, P. He, J. Yu, H. Yang, *Adv. Opt. Mater.* **2019**, *7*, 1801608.
- [34] T. J. Huisman, R. V. Mikhaylovskiy, J. D. Costa, F. Freimuth, E. Paz, J. Ventura, P. P. Freitas, Y. Mokrousov, Th. Rasing, A. V. Kimel, *Nat. Nanotechnol.* **2016**, *11*, 455.
- [35] T. J. Huisman, R. V. Mikhaylovskiy, A. Tsukamoto, Th. Rasing, A. V. Kimel, *Phys. Rev. B* **2015**, *92*, 104419.
- [36] P. Agarwal, R. Medwal, A. Kumar, H. Asada, Y. Fukuma, R. S. Rawat, M. Battiato, R. Singh, *Adv. Funct. Mater.* **2021**, *31*, 2010453.
- [37] F. Siegrist, J. A. Gessner, M. Ossiander, C. Denker, Y.-P. Chang, A. Guggenmos, Y. Cui, J. Walowski, U. Martens, J. K. Dewhurst, U. Kleineberg, S. Sharma, M. Schultze, *Nature* **2019**, *571*, 240.